Helium-ion Blistering in ITER-Grade and K-doped Tungsten under 20 keV He Ion Irradiation at 700 °C and the Effects of Microstructure and Crystallographic Orientation

Junhui Han[a], Woohyun Lim[a], Sangeun Kim[a], Hyung-Ha Jin[b], Dongwon Lee[b], Chansun Shin[*a]
[a]*Department of Materials Science & Engineering, Myongji University, Yongin 17058, Republic of Korea*
[b]*Korea Atomic Energy Research Institute, Daejeon 34057, Republic of Korea*

[*]*Corresponding author: c.shin@mju.ac.kr*

Keywords: Tungsten, K-doped tungsten, Helium ion irradiation, Blistering, Crystallographic orientation, EBSD

1. Introduction

Tungsten is a leading plasma-facing material for fusion divertors; however, helium exposure can induce pronounced surface and near-surface morphological changes, including blistering and helium-induced nanostructuring, which may degrade thermo-mechanical integrity and influence hydrogen isotope retention [1–3].

During normal divertor operation, tungsten surfaces are mainly exposed to low-energy ions in the scrape-off layer and edge plasma. Under these steady-edge conditions, ion energies are typically below a few hundred eV, and blistering is generally expected to be dominated by hydrogen isotopes (H/D/T) rather than helium. However, fusion reactors must also consider transient or localized conditions outside this low-energy regime. One important example is fast-ion loss, in which energetic ions escape confinement and strike plasma-facing components. In this context, Ueda et al. noted that high-energy helium ions (e.g., ripple-loss ions) can induce blistering through subsurface He bubble formation and crack development [4]. Such events may be intermittent and spatially localized, but they provide an implantation-like helium loading condition that is fundamentally different from low-energy He exposure associated with surface nanostructuring [4].

In parallel, potassium-doped tungsten (KdW) has been actively studied as an advanced alternative to conventional ITER-grade tungsten (IGW), particularly for improving high-temperature stability and irradiation tolerance. Nevertheless, a key gap remains in understanding how KdW responds to energetic He irradiation conditions relevant to implantation-driven blistering. In addition, although the mechanistic framework of keV-range He blistering in tungsten has been established in considerable detail, most studies have been conducted at or near room temperature. At elevated temperatures relevant to divertor operation, increased defect mobility and recovery, thermally activated bubble coarsening and coalescence, helium redistribution or release, and temperature-dependent plastic accommodation of the blister cap may significantly alter the onset, morphology, and failure mode of blistering. As a result, direct high-temperature keV-He data are needed to determine which aspects of the room-temperature mechanisms remain valid and how microstructure—including K-derived features in KdW—affects blister nucleation and evolution.

Motivated by this gap, the present study employs keV-range He irradiation under elevated-temperature conditions as a controlled surrogate for the energetic-He regime associated with fast-ion loss scenarios. By comparing blistering behavior in IGW and KdW under identical irradiation conditions, this work aims to clarify how microstructure governs blister nucleation, growth, and exfoliation in the implantation-driven regime. This approach also addresses the broader uncertainty in extrapolating current tungsten damage databases to the long-pulse, high-fluence, and multi-loading environments expected in DEMO and beyond [4].

2. Experimental

Polycrystalline IGW (rolled) and polycrystalline KdW (sintered) were used for He ion irradiation. Specimens were machined to 4 mm × 4 mm × 1 mm and mechanically polished (SiC papers and diamond suspensions), followed by colloidal silica polishing. A final electropolishing step was applied to improve surface quality for pre-irradiation microstructural characterization and EBSD analysis.

For each material, two specimens were prepared. One specimen was half-masked to produce irradiated and unirradiated regions on the same surface, enabling direct comparison of blistering behavior. The other specimen was covered with a TEM grid mask to create a square-patterned local irradiation map for spatial correlation of blister/crater distributions (Fig. 1).

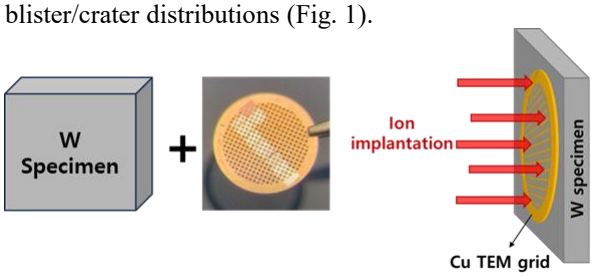

Fig. 1. Schematic illustration of He ion implantation using a TEM-grid-attached specimen

He irradiation was performed at 20 keV, 700 °C, and a fluence of 1×10^{18} ions/cm^2 to simulate an energetic He implantation condition. Depth profiles of implanted

He and irradiation damage were estimated by SRIM calculations using a displacement energy of 90 eV for W.

Pre-irradiation microstructures were characterized by SEM (BSE) and EBSD. SEM-BSE imaging was used to identify orientation contrast and fine dark-contrast surface features, while EBSD was used to analyze grain morphology, crystallographic orientation, and banded microstructural characteristics, particularly in IGW with respect to the rolling direction.

Post-irradiation surface damage was examined by SEM (SE mode). For half-mask specimens, observations were made across the irradiated/unirradiated boundary to compare blister formation and spatial distribution. For TEM-grid specimens, the square irradiation pattern was used to locally analyze blister/crater distributions. High-magnification SEM images were further used to classify surface features into dome-shaped blisters, partially opened blisters, and crater-like structures.

Direct EBSD indexing within the irradiated regions was limited by irradiation-induced surface roughening and damage. Therefore, for TEM-grid specimens, the square mask pattern was used as a positional reference, and the crystallographic orientations in irradiated squares were inferred from the continuity of orientation bands measured in adjacent unirradiated areas. This approach was used to assess the correlation between blister-concentrated regions and specific orientation bands.

3. Results and Discussion

Fig. 2 shows the SRIM-predicted depth profiles of displacement damage (dpa) and implanted He concentration (appm) in W for 20 keV He irradiation at a fluence of 1×10^{18} ions/cm^2. The calculated peak damage and peak He concentration were ~16 dpa at a depth of ~30 nm and ~1.6×10^{6} appm at a depth of ~60 nm, respectively. Both profiles are therefore confined to the near-surface region (within several tens of nanometers), indicating that the blister morphologies observed in Fig. 4 are controlled by near-surface He accumulation and irradiation-induced defect evolution. This near-surface localization is also consistent with implantation-driven blistering, where subsurface bubble/cavity formation and cap deformation dominate the surface response.

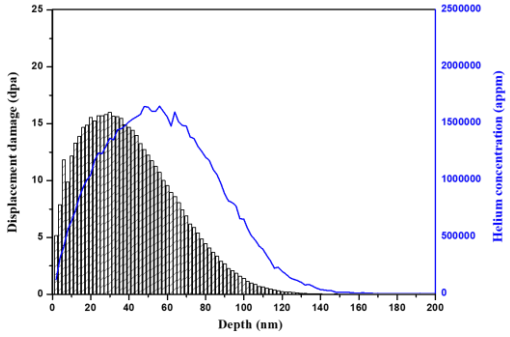

Fig. 2. SRIM-calculated depth profiles of implanted He concentration (right) and irradiation damage in W (left) for 20 keV He ion implantation at a fluence of 1×10^{18} ions/cm²

Fig. 3(a) and (b) show BSE images of the electropolished surfaces of the IGW and KdW specimens. In both materials, clear crystallographic orientation contrast is observed among grains in the polycrystalline microstructure, and fine dark-contrast spot features (pore-like or pull-out features) are distributed across the surface. IGW (Fig. 3a) exhibits elongated grains with a pronounced directional morphology associated with the rolling direction (RD), whereas KdW (Fig. 3b) shows a relatively more equiaxed grain structure. These characteristics are further supported by the EBSD result for IGW in Fig. 3(c), which reveals distinct orientation bands with widths of several tens of micrometers aligned along the RD. In addition, the EBSD map indicates an anisotropic banded microstructure containing substructures defined by low-angle grain boundaries within the bands.

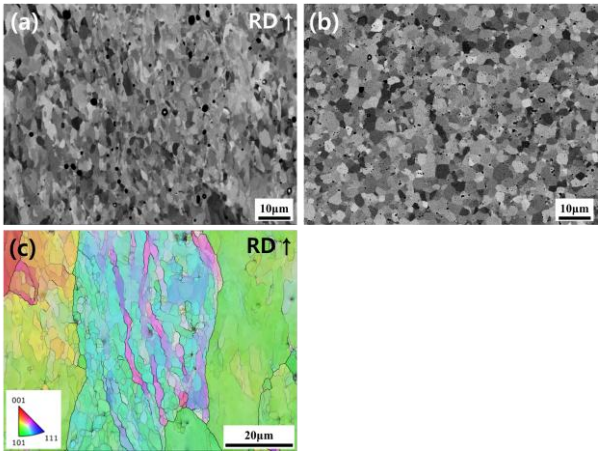

Fig. 3. (a) BSE image of the electropolished IGW surface, (b) BSE image of the electropolished KdW surface, and (c) EBSD map of IGW showing the banded microstructure along the rolling direction.

Fig. 4 shows SEM images of the half-mask specimens after He ion irradiation, including the boundary between the irradiated and unirradiated regions. Blisters were observed only in the irradiated regions, and clear differences in their spatial distributions were found between IGW and KdW.

In IGW, blister-rich regions (dotted outlines) were clearly distinguished from blister-sparse regions, and the concentrated blister zones exhibited a band-like spatial distribution with widths of several tens of micrometers. This trend is consistent with the banded microstructure and orientation distribution identified in IGW (Fig. 3). In contrast, KdW did not show the distinct band-like partitioning observed in IGW; instead, blisters were distributed more uniformly across the irradiated surface. These results suggest that differences in the pre-irradiation microstructures of IGW and KdW contribute to the distinct surface-damage distribution patterns after He irradiation.

High-magnification SEM images of both materials further revealed a range of blister morphologies, including dome-shaped blisters, partially opened blisters,

and crater-like features in which the blister caps had been fully removed. These morphologies are interpreted as representing different stages of blister growth and rupture (exfoliation).

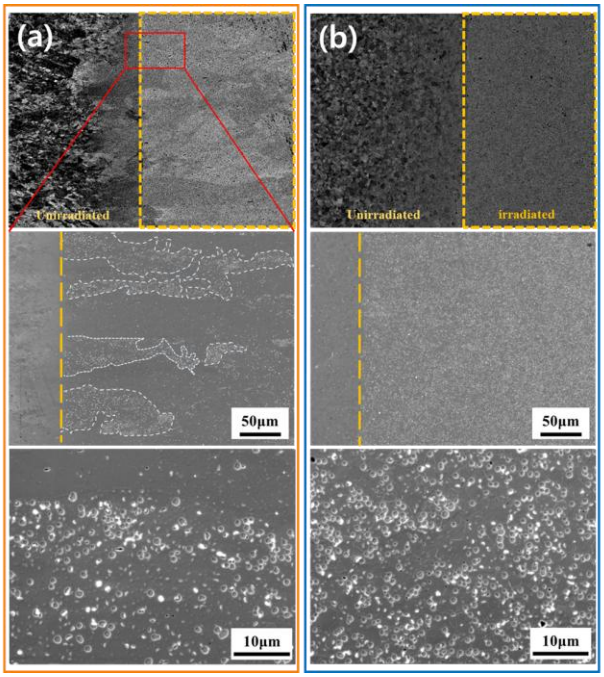

Fig. 4. SEM images of the irradiated/unirradiated boundary regions in the half-mask specimens after He ion irradiation: (a) IGW and (b) KdW.

A similar trend was observed in the TEM-grid–attached specimens, consistent with the half-mask results. In IGW (Fig. 5a), blistering was concentrated in specific regions, whereas in KdW (Fig. 5b), blisters were distributed relatively uniformly across the irradiated area. This difference in spatial distribution is consistent with the observations from the half-mask specimens and suggests a possible correlation with crystallographic orientation–dependent effects. Accordingly, additional EBSD analysis was performed to examine this relationship.

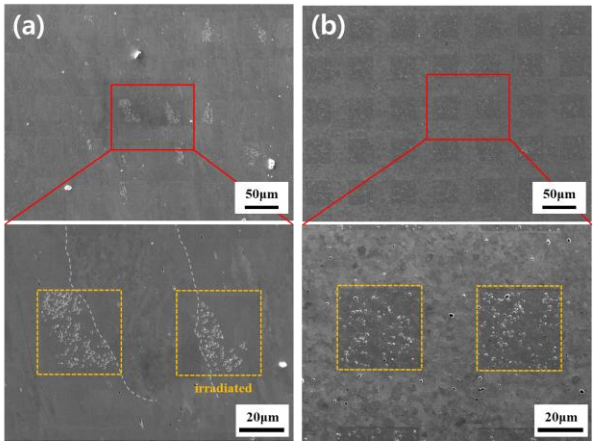

Fig. 5. SEM images of the TEM-grid–attached specimens after He ion irradiation: (a) IGW and (b) KdW.

During EBSD analysis, the ion-irradiated region showed poor crystallographic indexing due to irradiation-induced surface damage, which limited the direct acquisition of reliable orientation information. Therefore, the square irradiation pattern defined by the TEM grid mask was used as a positional reference, and the crystallographic orientations within the irradiated square regions were inferred from EBSD data obtained in the adjacent unirradiated area. This approach was used to evaluate the correlation between blister distribution and crystallographic orientation.

Fig. 6 shows that blister-concentrated regions tended to spatially overlap with the (001)-oriented band (red), whereas blisters were scarcely observed in other orientation bands, such as (101) and (111). These results suggest that the banded blister distribution observed in IGW is closely related to crystallographic orientation, and that blistering is likely to occur preferentially in near-(001) grain bands.

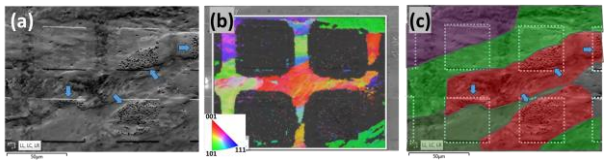

Fig. 6. EBSD-based analysis of the TEM-grid–attached IGW specimen: (a) FSE image acquired during EBSD analysis, (b) EBSD IPF orientation map overlaid on the FSE image, and (c) schematic overlay showing the inferred orientation bands and blister-concentrated regions in IGW.

One possible explanation for the pronounced blistering in the (001)-oriented band is that the high symmetry of this orientation and the activation of effective slip systems may provide a relatively greater capacity for accommodating surface deformation during and/or after irradiation [6]. In other words, orientation-dependent differences in plastic accommodation during He bubble growth and surface uplift may have influenced blister nucleation and subsequent growth.

In contrast, blistering in KdW was distributed relatively uniformly across the irradiated area, rather than being concentrated in specific regions as observed in IGW. This difference may be attributed to the processing route: unlike IGW, KdW is a sintered material fabricated without rolling, and therefore is expected to exhibit a more random grain-orientation distribution. In other words, because the pronounced banded, orientation-dependent microstructural anisotropy observed in IGW is much weaker in KdW, blistering in KdW appears more spatially uniform rather than locally concentrated.

However, as shown in Fig. 7, direct determination of crystallographic orientations within the irradiated region of KdW was also limited by poor EBSD indexing, similar to the IGW case (Fig. 6). In addition, the (001) orientation was not clearly indexed even in the adjacent unirradiated area. Therefore, at this stage, it is difficult to

conclude definitively whether blister formation in KdW is directly associated with the (001) orientation.

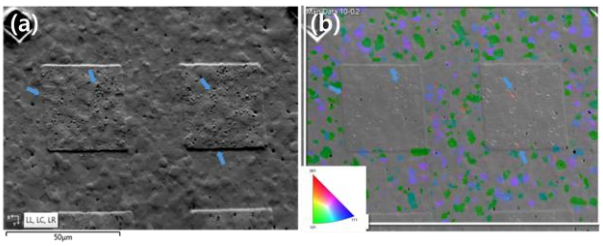

Fig. 7. EBSD-based analysis of the TEM-grid–attached KdW specimen: (a) FSE image acquired during EBSD analysis and (b) EBSD IPF orientation map overlaid on the FSE image.

A comparison of the crater sizes in the irradiated regions of the TEM-grid–attached specimens showed that the mean crater area in IGW was 0.69 μm², approximately 58% larger than that in KdW as shown in Fig. 8. This result indicates that, under identical irradiation conditions, KdW tends to form smaller craters than IGW.

If blistering in KdW is also preferentially associated with a specific crystallographic orientation (e.g., near-(001)), as suggested for IGW, the K-derived bubbles/features in KdW may act as He trapping sites and thereby modify local He accumulation and bubble-growth behavior. In that case, the craters formed after blister rupture could remain smaller than those in IGW. However, the EBSD results in Fig. 7 do not allow a clear confirmation of a direct correlation between blistering in KdW and the (001) orientation. Therefore, this interpretation should be regarded as a plausible working hypothesis rather than a definitive conclusion. To verify the orientation–blister correlation more rigorously, additional experiments are needed in which EBSD is first performed on the same region prior to ion irradiation, followed by irradiation at the identical location and direct comparison of the resulting blister/crater distributions.

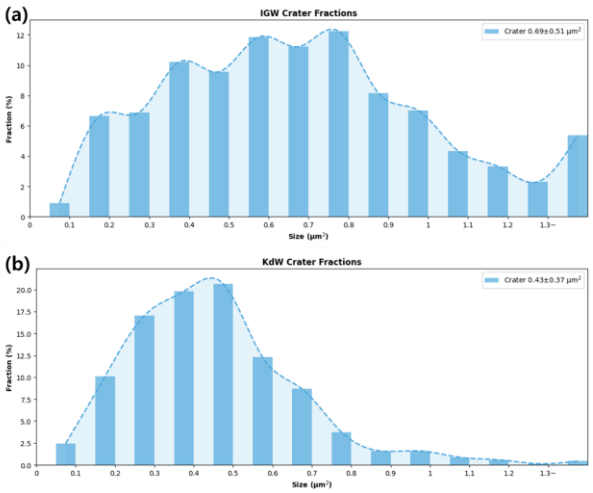

Fig. 8. Crater size distribution plots for the TEM-grid–attached specimens: (a) IGW and (b) KdW.

4. Conclusion

In this study, the surface damage behavior of IGW and KdW under 20 keV He ion irradiation was compared, and the results show that differences in pre-irradiation microstructure and crystallographic orientation distribution are directly reflected in blistering behavior. In IGW, localized blister concentration corresponding to the rolling-induced banded microstructure was observed, whereas KdW exhibited a relatively uniform blister distribution across the irradiated region. Based on EBSD-assisted orientation inference, the blister-concentrated regions in IGW tended to overlap with near-(001) orientation bands, suggesting a strong orientation dependence of blister formation. In addition, the mean crater area in IGW was approximately 58% larger than that in KdW, indicating that crater formation in KdW remained relatively smaller under identical irradiation conditions. A possible explanation is that K-derived bubbles/features in KdW modified local He accumulation and bubble growth by acting as trapping sites; however, this interpretation remains a working hypothesis at this stage. Future work should include direct EBSD–SEM correlation on the same locations before and after irradiation to quantitatively verify the orientation–blister relationship and clarify the role of K-derived features in blister evolution.

REFERENCES

[1] Y. Ueda, H.T. Lee, N. Ohno, S. Kajita, N. Yoshida, R. Doerner, G. De Temmerman, V. Alimov, G. Wright, Helium effects on tungsten surface morphology and deuterium retention, Journal of Nuclear Materials, 442 (2013) S267-S272

[2] R. Gonzalez-Arrabal, A. Rivera, J. M. Perlado, Limitations for tungsten as plasma facing material in the diverse scenarios of the European inertial confinement fusion facility HiPER: Current status and new approaches, Matter and Radiation at Extremes, 5 (2020) 055201

[3] Laima Luo, Jing Shi, Jinshan Lin, Xiang Zan, Xiaoyong Zhu, Qiu Xu, Yucheng Wu, Microstructure and performance of rare earth element-strengthened plasma-facing tungsten material, Scientific Reports, 6 (2016) 32701

[4] Y. Ueda, J.W. Coenen, G. De Temmerman, R.P. Doerner, J. Linke, V. Philipps, E. Tsitrone, Research status and issues of tungsten plasma facing materials for ITER and beyond, Fusion Engineering and Design, 89 (2014) 901-906

[5] Y.-R. Lin, S.J. Zinkle, C.J. Ortiz, J.-P. Crocombette, R. Webb, R.E. Stoller, Predicting displacement damage for ion irradiation: Origin of the overestimation of vacancy production in SRIM full-cascade calculations, Current Opinion in Solid State and Materials Science, 27 (2023) 101120

[6] C. Fan, S. Pan, X. Hu, B. He, M. Huang, Mechanisms of helium irradiation blistering and surface deformation in tungsten, Acta Materialia, 254 (2023) 118993.